Regional map of molecular water at high southern latitudes on the Moon using 6 μm data from the Stratospheric Observatory For Infrared Astronomy

Casey I. Honniball[1], Paul G. G. Lucey[2], Anicia Arredondo[3], William T Reach[3], and Erick Malaret[4]

[1]NASA Goddard Space Flight Center
[2]University of Hawaii at Manoa
[3]USRA
[4]ACT Corp.

November 24, 2022

Abstract

A map of surface molecular water was derived from long slit spectroscopy of the south polar region of the Moon using the Faint Object infraRed CAmera for the SOFIA Telescope (FORCAST) spectrometer on the Stratospheric Observatory for Infrared Astronomy (SOFIA). Mean water abundances detected are about 250 μg/g over that of a mare reference surface at Mare Fecunditatis. Water abundances are locally anticorrelated with temperature and latitude. The distribution of water is consistent with derivation of water from pre-existing hydroxyl subsequently trapped in impact glass, provided hydroxyl increases with latitude as some models and measurements suggest. The detected water cannot be in equilibrium with the exosphere because insufficient water is present to maintain the surface abundance. The data are also consistent with a high latitude water-bearing mineral host that may be a precursor to recently detected high latitude hematite.

Regional map of molecular water at high southern latitudes on the Moon using 6 µm data from the Stratospheric Observatory For Infrared Astronomy

C. I. Honniball[1], P. G. Lucey[2], A. Arrendando[3], W. T. Reach[3] and E. R. Malaret[4]

[1]NASA Goddard Space Flight Center, Greenbelt, MD, USA. [2]Hawai‘i Institute of Geophysics and Planetology, University of Hawai‘i at Mānoa, Honolulu, HI, USA. [3]Universities Space Research Association, Columbia, MD, USA. [4]Applied Coherent Technology, Herndon, VA, USA.

Corresponding author: Casey Honniball (casey.i.honniball@nasa.gov)

Key Points:

- SOFIA+FORCAST confirms the presence of water emission in the South Polar Region of the Moon.
- Small maps of water emission are presented that begin to enable tests of various hypotheses for water formation and variation.
- Observations suggest the water cannot migrate and instead is trapped within impact glasses or in a mineral-based host.

Abstract

A map of surface molecular water was derived from long slit spectroscopy of the south polar region of the Moon using the Faint Object infraRed CAmera for the SOFIA Telescope (FORCAST) spectrometer on the Stratospheric Observatory for Infrared Astronomy (SOFIA). Mean water abundances detected are about 250 µg/g over that of a mare reference surface at Mare Fecunditatis. Water abundances are locally anticorrelated with temperature and latitude. The distribution of water is consistent with derivation of water from pre-existing hydroxyl subsequently trapped in impact glass, provided hydroxyl increases with latitude as some models and measurements suggest. The detected water cannot be in equilibrium with the exosphere because insufficient water is present to maintain the surface abundance. The data are also consistent with a high latitude water-bearing mineral host that may be a precursor to recently detected high latitude hematite.

Plain Language Summary

If water is present in sufficient quantities on the Moon, it may be an important resource for space exploration as it can be used to make rocket fuel and sustain human presence. The water molecule on the illuminated surface of the Moon can be detected using a unique spectral signature that is obscured from telescopes on Earth's surface by water vapor in the atmosphere. The NASA/DLR Stratospheric Observatory for Infrared Astronomy (SOFIA) is a large telescope on a 747 aircraft that operates high in the stratosphere above 99% of the water vapor, and so can detect the infrared thermal emission from water on the Moon's surface. Near the South Pole, we produced a map of water emission that shows water is present at a few hundred parts per million, and is inversely correlated with surface temperature. This is consistent both with the behavior of water free to migrate on the surface, and water bound up in glass from meteorite impacts. However, the amount of water we find probably cannot be freely exchanging with the Moon's tenuous exosphere because it would require much more water in the exosphere than has been measured.

1 Introduction

The water molecule is a key compound for understanding the interaction of airless planetary surfaces with the space environment. This interaction is often termed "space weathering," denoting that surfaces evolve with space exposure in a manner analogous to terrestrial geologic weathering (Pieters et al., 2000). The Moon's surface that is exposed to space weathering is the lunar regolith which is poorly sorted but largely fine grained with a mean grain size of 60 µm (McKay et al., 1991). It is a product of pulverization of the lunar surface by billions of years of meteorite impacts of all sizes. The principal agents of space weathering in our Solar System are the solar wind and micrometeorites (Pieters et al., 2000). The solar wind is a moderate energy plasma that emanates from the solar corona composed largely of protons (H+), but also the nuclei of other elements, as well as electrons (Meyer-Vernet, 2007). The solar wind implants hydrogen and other elements a few nanometers into the surfaces of lunar grains forming hydroxyl (OH; Zeller et al., 1966), as well as sputtering their surfaces, resulting in vapor deposited coatings on neighboring grain surfaces (Keller and McKay, 1997). Micrometeorites, defined as those impactors less than 1 cm (Grun et al., 2001), melt and vaporize the regolith target producing vapor deposited coatings, as well as melt welded aggregates of glass and mineral fragments called agglutinates (McKay et al., 1991).

Water molecules have two principal styles of emplacement in the space weathering process: They can be directly introduced into the lunar environment, or synthesized from solar wind hydrogen. A fraction of the population of micrometeorites and other small impactors are water-bearing, containing minerals that include the water molecule in their structures (Hanner and Zolensky, 2010). A portion of this water is promptly released on impact, but a substantial fraction, on the order of 1/3, can be retained in impact glass produced during the impact (Daly and Schultz, 2018). The energy of micrometeorite impact can also facilitate synthesis of water from a hydroxyl precursor (Zhu et al., 2019). Hydroxyl was proposed to be formed in the lunar surface from a reaction of solar wind hydrogen and oxygen in lunar minerals (Zeller et al., 1966). Zhu et al. (2019) showed that a particulate surface containing pre-existing hydroxyl could form and release water in the vapor phase with stimulations of micrometeorite impacts using laser irradiation. Presumably the water formed during impact could also be trapped in the impact glass produced, this time originating in the target rather than the impactor. Bennett et al. (2013) and Jones et al. (2018) showed that thermal energy from high lunar noontime temperatures could produce water from recombinant desorption of adjacent hydroxyls that would react to form water and hydrogen, both released into the lunar exosphere.

While characterizing the behavior and origin of water is important to understanding the planetary process that is space weathering, it is of topical importance owing to the value of water for the progress of space exploration. Water ice is known to occur in permanently shadowed regions of the lunar poles that feature sustained temperatures below 100 K (Li et al., 2018, Hayne et al., 2015), and is a potential resource for many aspects of space exploration. As with any resource, an understanding of its formation aids its use as a resource. One commonly assumed mechanism for supply of water to the poles is by cold trapping of water vapor from the lunar exosphere, but the viability of this mechanism is a matter of research.

The only direct evidence of the water molecule in the lunar environment outside ice detections in regions of permanent shadow comes from two experiments. Mass spectroscopic measurements in lunar orbit from the Neutral Mass Spectrometer on the Lunar Atmosphere and Dust Environment Explorer (LADEE) spacecraft that detected water associated with meteor showers (Benna et al., 2019) , perhaps reflecting the Zhu et al. (2019) or Daly and Schultz (2018) processes, and placed an upper limit of <0.1 molecules per cubic centimeter as the background away from meteor stream events. Infrared emission at the fundamental water vibration at 6 μm from surface water was found by Honniball et al. (2020) using the Stratospheric Observatory for Infrared Astronomy (SOFIA) (Young et al., 2012). Other than these measurements, there are few constraints on the origin, evolution and ultimate fate of water in the lunar environment.

In this paper we describe additional measurements of lunar surface water by SOFIA that confirm the presence of water emission, and produced small maps of water emission that begin to enable tests of various hypotheses for water formation and variation.

2 Data and Methods

Spectral data were obtained with the Faint Object infraRed CAmera for the SOFIA Telescope (FORCAST) on SOFIA (Herter et al., 2018). The high operational altitude of SOFIA situates it above most of the water vapor in the terrestrial atmosphere enabling unique access to the 6 μm wavelength region, which is obscured from groundbased observatories by water vapor absorption. FORCAST can be operated as a long slit spectrograph using a grism in its optical train and employs a 256 x 256 Si Blocked-Impurity-Band infrared focal plane array for detection. We used the FORCAST G063 grism with a 2.4 by 191 arcsecond slit sampled by 249 pixels with 0.768

arcsecond pixel height to obtain spectra from 5 to 8 μm with a spectral resolution of 180 ($\boldsymbol{\Delta\lambda/\lambda}$, or about 12 nm). The spatial resolution of each pixel at the lunar center of disk is about 4.8 x 1.5 km.

A technical goal of the observations was to demonstrate FORCAST could be used as an imaging spectrometer by scanning the slit across the lunar surface as the detector was read out to form pushbroom scan images. By the end of the flight the SOFIA telescope operators were able to advance the slit by approximately one slit width per frame.

A region surrounding the southern polar crater Moretus (70.6˚S, 6.4˚W) was chosen for measurement. This region is adjacent to Clavius crater observed by Honniball et al. (2020) broadening coverage of the Moon, but still at high latitude with the expectation that molecular water might be present. This region is known to have high values of "total water" (the sum of molecular water and hydroxyl) based on measurements using the Moon Mineralogy Mapper on the Chandrayaan-1 lunar orbiter (Li and Milliken, 2017). A near equatorial portion of Mare Fecunditatis was chosen as the reference location, and this mare site's distance from the terminator ensured higher temperatures than the high latitude Moretus region on the assumption that a high temperature equatorial site would contain less water than a polar site. A total of 93 frames of south polar region were obtained, and 32 frames of reference data.

On source integration times of 8.6 seconds per frame were used for both the Moretus polar site and the equatorial reference site. The zenith angle of the observations ranged from 58.91˚ to 61.71˚ during data acquisition and the aircraft traveled ~22˚ in terrestrial longitude maintaining an altitude between 39,990 ft. and 42,028 ft. Supplementary Table S1 summarizes the observation conditions during each observation segment.

Data were placed in the lunar cartographic system with a combination of celestial coordinates reported by the SOFIA telescope control system, and refinement using guider images obtained with the visible range Focal Plane Imager (FPI). Synthetic simulated FPI images of the Moon were produced using Lunar Reconnaissance Orbiter Camera, Wide Angle Camera data draped on Lunar Reconnaissance Orbiter topographic data with lighting rendered to simulate the appearance of the FPI images at the time of data acquisition. The FPI images are then correlated with the simulated data to determine the spatial offsets of the FPI images from the celestial coordinate system. Finally, using predetermined position of the FORCAST slit on the FPA, the corners of each slit pixel are assigned a latitude and longitude and can be mapped using standard projection (Figure S1).

Calibration and processing of the data follows the methodology of Honniball et al. (2020) with a few improvements to the atmospheric removal and corrections to residual artifacts that are further described in the supplementary information.

4 Results

Emission features near 6 μm were observed in all spectra of the region surrounding Moretus crater reduced as ratios of south polar data relative to the mare reference site in Mare Fecunditatis (Figure 1). Each 6 μm water emission feature was fit with a Gaussian to characterize centers and widths. The centers and widths of the bands are consistent with water bearing crystalline hydrates (Falk, 1984), hydrated meteorites (Takir et al., 2019), a sample of water bearing glass (Li, 2017; Shimizu et al., 2015) and the data collected of the Clavius region as reported in Honniball et al. (2020) (Figure 2). Temperatures derived from the radiance spectra are consistent with expectations for this latitude and lunar time of day based on time of day bolometric temperature measurements derived from the LRO Diviner Lunar Radiometer (Williams et al., 2017; Figure S2) lending confidence to the radiance calibration.

Observed emission peak heights were converted to water concentration (µg/g) using the calibration of Honniball et al. (2020.) Emission peak heights were defined as the average emissivity between +/- 0.04 µm around the 6 µm band center found by the Gaussian fits relative to a linear continuum defined at 5.8 to 5.9 µm and 6.3 to 6.4 µm specifically avoiding the 6 µm band. Emission data are converted to apparent emissivity, then to reflectance via Kirchhoff's law in order to apply the Honniball et al. (2020) calibration which used particulate samples measured in reflectance. Water concentrations range from 100 to 400 µg/g , consistent with those reported by Honniball et al. (2020) for the nearby Clavius region (Figure S3).

Only limited spatial analysis was possible by Honniball et al. (2020) owing to the small number of slit observations, but the new data reported here are formatted as images to allow consideration of spatial relationships. Figure 3a shows the mean flux from 5 to 8 µm georeferenced and mapped onto a lunar background image. Craters and other topographic features are readily apparent in the georeferenced image. Throughout the wavelengths covered by the measurements, lunar radiance is dominated by thermal emission, and temperature is largely dominated by the effect of local slopes; surface temperatures are dictated by the angle of the surface normal to the Sun, resulting in images that appear very similar to visible images of the Moon obtained at moderate and large phase angles. The images feature a roughly north-south gradient in flux consistent with proximity to the subsolar point (0.6° N, 21.25° E) that was north and slightly to the east of Moretus

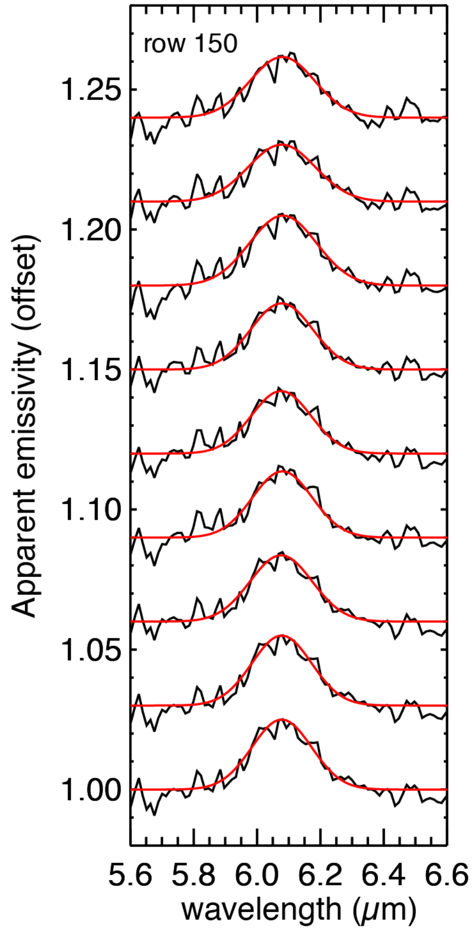

Figure 1: Representative spectra of the Moretus region with Gaussian fits superimposed.

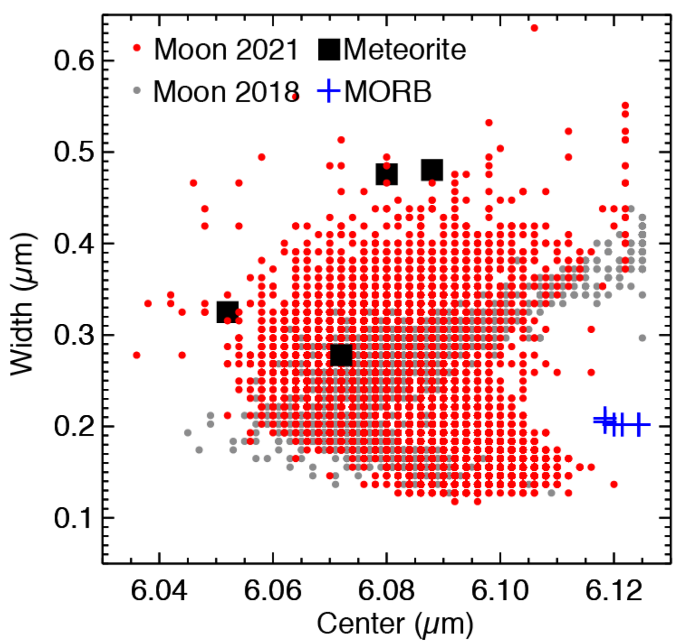

Figure 2: Emission peak centers vs. peak widths for measurements presented here (red), SOFIA measurements from Honniball et al. (2020; gray), hydrated meteorites (black), and silicate glass (MORB: Mid-Ocean Ridge Basalt; blue).

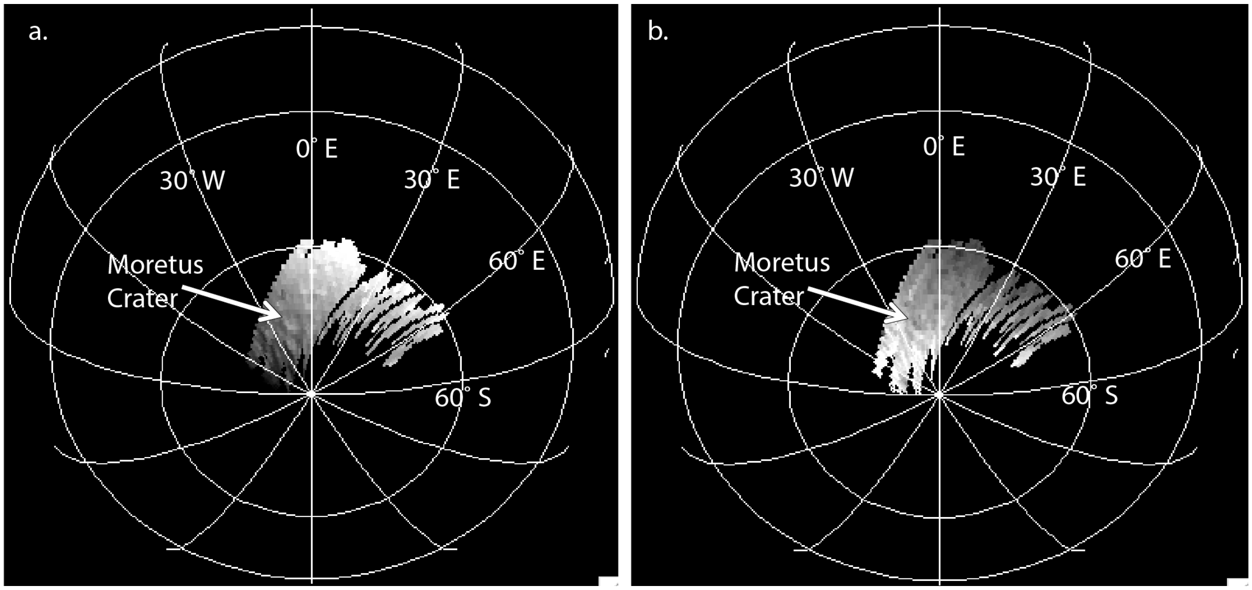

Figure 3: Orthographically rectified images of average flux (a) and emission peak height (b).

longitude, and modulation by temperature variations due to local slopes.

An image of the emission peak height is shown in Figure 3b. There is a moderate inverse correlation of peak height and flux (Figure 4), which indicates a control by temperature or latitude, where latitude is a proxy for the average or maximum temperature of the site.

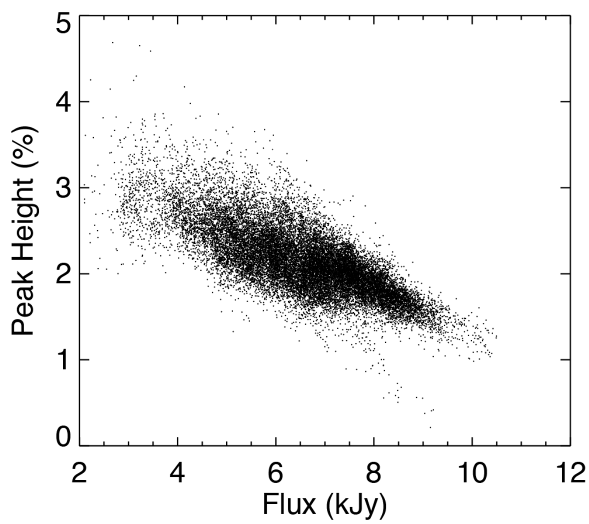

Figure 4: Correlation of peak height with average flux.

5 Discussion

These new measurements confirm the findings of Honniball et al. (2020) that the lunar south polar region features about 200 μg/g molecular water relative to a low latitude mare site based on observations of a 6 μm surface emission feature.

There are three reservoirs that might host the detected water molecules: adsorbed on silicate surfaces, trapped or dissolved in silicate glass, or chemically bound to a mineral (Dyar et al., 2010; Daly and Schultz, 2018; Lucey et al., 2021). Water physically adsorbed on the surface of silicate grains is the surface state of water that can potentially migrate through the exosphere to the poles via hopping ballistically and randomly across the surface, known as ballistic migration (Watson et al., 1961). In this case water in the exosphere lacking sufficient thermal energy and direction to escape will return to the surface on a ballistic trajectory. If the water molecule survives the impact with the surface (which is not assured; Jones et al., 2018), then it will remain until thermal agitations of the surface and the molecule give it enough energy to overcome the weak van der Waals bonds between the molecule and the silicate grain surface (physisorption). While trapped on the surface, the molecule is able to emit thermal radiation which is enhanced by the high emissivity at the water fundamental.

The second potential reservoir for detected surface water is in silicate glass as proposed by Honniball et al. (2020) to explain their water detections. Per Daly and Schultz (2018), water derived from projectiles can remain in glass formed from the impact with reasonably high efficiency (10s of percent of impactor water preserved). Presumably the Zhu et al. (2019) process of water synthesis from hydroxyl aided by impact energy would also result in some amount of water trapped in glass as opposed to water released as vapor. Hydroxyl might also be expected to occur in the glass. Liu et al. (2012) detected either water or hydroxyl in the small impact melt bodies common in lunar soils (agglutinates); their FTIR measurements used the "total water" band at 3 µm and did not include 6 µm measurements, and their SIMS measurements detect hydrogen so the presence of the water molecule is not confirmed.

The third possibility is that the water is bound within the structure of a mineral. There are no minerals containing molecular water in the lunar sample collection, however, at high latitudes (>60˚) the iron oxide hematite, also absent in the sample collection, was detected. For example, Li et al. (2020) suggested that this hematite might be formed from dehydration of a hydrated iron oxide precursor (hydrated iron oxide). A hydrated precursor was invoked to explain the observation that the hematite is limited to high latitudes where the 3 µm total water band persists throughout the lunar day, suggesting some influence of hydration on hematite formation.

Honniball et al. (2020) dismissed the possibility of physisorbed water based on results of Poston et al. (2015) that suggested the mean residence time of water for the Clavius data was only a few seconds. We probe the possibility of physically adsorbed water further with these new data, and arrive at the same conclusion.

The upper limit on the equatorial exospheric water abundance provided by Benna et al. (2019) is a strong constraint on the viability of surface adsorbed water. Considering a 1-dimensional model, the abundance of water in the exosphere relative to the abundance on the surface is the ratio of the mean ballistic flight time and the surface residence time of a water molecule. The former is a function of the surface temperature that provides the energy to propel a molecule into the exosphere and the latter is a function of surface temperature and the energy of desorption of water from a silicate surface. The time of flight ($\boldsymbol{T_f}$) is:

$$\boldsymbol{T_f = 2v * \frac{\sin(\theta)}{g}} \qquad \text{eq. 1}$$

where $\boldsymbol{\theta}$ is the ejection angle, $\boldsymbol{v}$ is the speed of ejection and $\boldsymbol{g}$ is the gravitational acceleration of the body. The mean speed of ejection ($\boldsymbol{v}$) in the z-axis is:

$$\boldsymbol{v = \sqrt{\frac{2RT}{M}}} \qquad \text{eq. 2}$$

where $\boldsymbol{R}$ is the gas constant, $\boldsymbol{T}$ is the temperature (K) and $\boldsymbol{M}$ is the molecular weight (kg/mol). For a 300K surface with an average ejection angle of 45 degrees, the time of flight is 91 s, which we can safely round to 100 s.

The surface residence time at 300K is an exponential function of the activation energy of desorption. Estimates vary widely, with a low value of less than 1 eV from Jones et al. (2021) and a high of 1.3 eV from Hendrix et al. (2019) owing to the exponential nature of the residence time, the ratio of exospheric to surface mass varies from over 3 at 0.8 eV, to 1×10^{-8} at 1.3 eV. We can estimate the exchangeable surface mass from the 200 μg/g water concentration from our calibration. Equating the surface sensed by the thermal measurements with the exchangeable mass of water, with the mean grain size of the lunar surface of about 60 μm, and the sensing depth is on the order of a few grains. Taking the sensing depth then as ~100 μm, the mass of exchangeable water per square centimeter is about 10 micrograms per square centimeter assuming a grain density of 2.85 g/cc (Kiefer et al., 2012). Using the mass ratios above, the exospheric density at one scale height (86 km) would range from 10^{18} to $3x10^{9}$ molecules per cubic centimeter. These exospheric densities are extremely large, far over the upper limit provide by Benna et al. (2019) from in situ mass spectroscopic measurements. To meet the upper limit imposed by Benna et al. (2019) the activation energy of desorption would have to be ~1.8 eV, far above any previous estimate, and above any consideration of water as a volatile (surface residence times would exceed 10^{6} years). This order of magnitude calculation supports the contention by Honniball et al. (2020) that the water sensed by SOFIA+FORCAST cannot be that of migrating water.

Our data are not inconsistent with a mineral-based host of molecular water. Li et al. (2020) detected anhydrous iron oxide (hematite) at high lunar latitudes (>60˚), but suggested that the coincidence of high total water abundance, low solar wind hydrogen fluence and the presence of extremely fine-grained iron metal common in lunar soil might produce a hydrated iron oxide precursor (FeOOH) that later dehydrates to hematite (the common potential precursors are much less detectable than hematite in near-IR data explains their lack of detection). If there is a relationship, the mineral present would likely be ferrihydrite (water bearing iron oxide). Our data is limited to latitudes above 60˚S, but suggest strong tests are possible in future observations that span lower latitudes.

However, the most likely host of the detected water is silicate impact glass as suggested by Honniball et al. (2020). This possibility is supported by the impact experiments of Daly and Schultz (2018), and the water synthesis experiments of Zhu et al. (2019) and does not invoke speculative chemical reactions.

Our results have implications for models or hypotheses for molecular water distribution. Any model that correlates molecular water with solar wind fluence is inconsistent with our observations. For example, if hydroxyl were correlated with fluence, then presumably micrometeorite impact would convert a portion of this hydroxyl to molecular water, a portion of which could in turn be sequestered in impact glass. The ratio of solar wind fluence between our reference and the Moretus site is between 5 and 15 using the equations and assumptions of Johnson et al. (1999), whereas water abundance is ~200 μg/g higher at the southern Moretus site. This is the reverse of expectation if solar wind fluence dominated water concentrations.

However, our data are consistent with a model by Jones et al. (2018) where hydroxyl is eroded from low latitudes through recombinant desorption of surface correlated hydroxyl to water and hydrogen released into the exosphere, facilitated by high equatorial midday temperatures. For this model to be consistent with our data, we must assume that molecular water is formed per Zhu et al. (2019) from pre-existing hydroxyl and then trapped in impact glass, and so follows the evolved hydroxyl distribution.

Owing to the high correlation of latitude and temperature in our data, we do not constrain models that require water to respond to the instantaneous temperature, though ballistic migration appears inconsistent with the exospheric limits imposed by LADEE and the surface abundance we measure.

6 Conclusions

We have verified the observation that excess molecular water emission is found at high lunar latitudes. We have strengthened the correlation of temperature or latitude with molecular water abundance, but this set of data cannot distinguish which parameter dominates. A simple model suggests that ballistic migration of water through the exosphere is not consistent with most of the detected water being exchangeable with the exosphere, though does not rule out a small amount. Our data are not inconsistent with a mineral host of the molecular water, but we suggest an impact glass host is the most likely. Models that result in hydroxyl abundances correlated with solar wind fluence seem ruled out, but this assumes micrometeorites will trap molecular water in impact glass and freeze in a distribution similar to hydroxyl. A hybrid of the Jones et al. (2018) model that results in strong latitude increases in hydroxyl toward the poles, and trapping of water synthesized from hydroxyl into impact glass is consistent with our data.

Further observations can create robust tests of these models. The variation of water emission with time of day at any latitude constrains the ballistic migration hypothesis, and any other model that forms molecular water proportional to instantaneous temperature, so time of day observations are critical, including at low latitudes since 3 μm observations suggest that hydration increases toward the terminator.

Acknowledgments

This work was based on observations made with the NASA/DLR Stratospheric Observatory for Infrared Astronomy (SOFIA). SOFIA is jointly operated by the Universities Space Research Association, Inc. (USRA), under NASA contract NNA17BF53C, and the Deutsches SOFIA Institut (DSI) under DLR contract 50 OK 0901 to the University of Stuttgart. Financial support for P.G.L. and C.I.H. for this work was provided by NASA through award # SOF 08-0132 issued by USRA and by the NASA Solar Systems Observations Grant 80NSSC21K0288. Financial support for A.A. for this work was provided by NASA through award # SOF 06-0010 issued by USRA. C.I.H. is also supported by an appointment to the NASA Postdoctoral Program at the NASA Goddard Space Flight Center administered by Universities Space Research Association under contract with NASA.

Open Research

The spectral data that support the plots within this paper and other findings of this study are publicly available from the SOFIA Data Cycle System hosted by the Infrared Science Archive hosted by the Infrared Processing & Analysis Center (IPAC)) at https://irsa.ipac.caltech.edu. Please go to the SOFIA Archive, select 'Solar System Object' and search for 'Moon' observations, then select the FORCAST tab to locate the data.

References

Benna, M., Hurley, D. M., Stubbs, T. J., Mahaffy, P. R. & Elphic, R. C. (2019), Lunar soil hydration constrained by exospheric water liberated by meteoroid impacts. *Nat. Geosci.* 12, 333.

Bennett C.J., Pirim, C., Orlando, T.M., (2013), Space-weathering of solar system bodies: A laboratory perspective. *Chemical reviews*. Dec 11;113(12):9086-150.

M. Clarke et al. (2021), Guest Observer Handbook for FORCAST Data Products, https://www.sofia.usra.edu/sites/default/files/USpot_DCS_DPS/Documents/FORCAST_data_handbook.pdf

Daly, R. T. & Schultz, P. H. (2018), The delivery of water by impacts from planetary accretion to present. *Sci. Adv*. 4, 1–11.

Dyar, M.D., Hibbitts, C.A., Orlando, T.M. (2010), Mechanisms for incorporation of hydrogen in and on terrestrial planetary surfaces. *Icarus*. Jul 1;208(1):425-37.

Falk, M. (1984), The frequency of the H-O-H bending fundamental in solids and liquids. *Spectrochim. Acta* 40A, 43–48.

Grün, E., Horanyi, M., Sternovsky, Z., (2011), The lunar dust environment. *Planetary and Space Science.* Nov 1;59(14):1672-80.

Hanner, M.S., Zolensky, M.E., (2010), The mineralogy of cometary dust. *InAstromineralogy*, pp. 203-232. Springer, Berlin, Heidelberg.

Hendrix, A. R., Hurley, D. M., Farrell, W. M., Greenhagen, B. T., Hayne, P. O., Rutherford, K. D., et al. (2019). Diurnally Migrating Lunar Water: Evidence From Ultraviolet Data. *Geophysical Research Letters*, 46(5), 2417–2424.

Herter, T.L., Adams, J.D., De Buizer, J.M., Gull, G.E., Schoenwald, J., Henderson, C.P., Keller, L.D., Nikola, T., Stacey, G., Vacca, W.D., (2012), First science observations with SOFIA/FORCAST: the FORCAST mid-infrared camera. *The Astrophysical Journal Letters*. Mar 29;749(2):L18.

Honniball, C. I., Lucey, P. G., Li, S., Shenoy, S., Orlando, T. M., Hibbitts, C. A., Hurley, D. M. and Farrell, W. M., (2020), Molecular water detected on the sunlit Moon by SOFIA, *Nature Astron*, 5 121 –127. https://doi.org/10.1038/s41550-020-01222-x

Johnson, J.R., Swindle, T.D., Lucey, P.G., (1999), Solar-Wind-Implanted Volatiles in the Lunar Regolith. *New Views of the Moon 2: Understanding the Moon Through the Integration of Diverse Datasets*. Jan:29.

Jones, B.M., Aleksandrov, A., Hibbitts, C.A., Orlando, T.M., (2021), Thermal evolution of water and hydrogen from Apollo lunar regolith grains. *Earth and Planetary Science Letters*. Oct 1;571:117107.

Jones, B. M., Aleksandrov, A., Hibbitts, K., Dyar, M. D., & Orlando, T. M. (2018). Solar wind-induced water cycle on the Moon. *Geophysical Research Letters*, 45, 10,959–10,967. https://doi.org/10.1029/2018GL080008

Keller, L.P. and McKay, D.S., (1997), The nature and origin of rims on lunar soil grains. *Geochimica et Cosmochimica Acta*. Jun 1;61(11):2331-41.

Kiefer, W.S., Macke, R.J., Britt, D.T., Irving, A.J., Consolmagno, G.J., (2012), The density and porosity of lunar rocks. *Geophysical Research Letters*. Apr;39(7).

Li, S., Lucey, P. G., Fraeman, A. A., Poppe, A. R., Sun, V. Z., Hurley, D. M., & Schultz, P. H. (2020). Widespread hematite at high latitudes of the Moon. *Science Advances*, 6(36), eaba1940. https://doi.org/10.1126/sciadv.aba1940

Li, S. (2017). Water on the Lunar Surface as Seen by the Moon Mineralogy Mapper: Distribution, Abundance, and Origins. *Brown University, PhD Dissertation* (pp. 1–311)

Li, S. & Milliken, R. E., (2017). Water on the surface of the Moon as seen by the Moon Mineralogy Mapper: Distribution, abundance, and origins. *Science Advances*, 3(9), e1701471.

Liu, Y. et al. (2012), Direct measurement of hydroxyl in the lunar regolith and the origin of lunar surface water. *Nature Geoscience*, 5, 779-782.

Lord, S.D., (1992), A new software tool for computing Earth's atmospheric transmission of near- and far-infrared radiation. Vol. 103957. *Ames Research Center*.

McCord, T. B., Taylor, L. A., Combe, J. P., Kramer, G., Pieters, C. M., Sunshine, J. M., & Clark, R. N. (2011). Sources and physical processes responsible for OH/H2O in the lunar soil as revealed by the Moon Mineralogy Mapper (M3). *Journal of Geophysical Research: Planets*, 116, 1–22.

McKay, D.S., Heiken, G., Basu, A., Blanford, G., Simon, S., Reedy, R., French, B.M., Papike, J., (1991), The lunar regolith. *Lunar sourcebook*. 567:285-356.

Meyer-Vernet N., (2007), Basics of the solar wind. *Cambridge University Press*; Jan 18.

Pieters, C.M., Taylor, L.A., Noble, S.K., Keller, L.P., Hapke, B., Morris, R.V., Allen, C.C., McKay, D.S., Wentworth, S., (2000), Space weathering on airless bodies: Resolving a mystery with lunar samples. *Meteoritics & Planetary Science*. Sep;35(5):1101-7.

Poston, M. J. et al. (2015), Temperature programmed desorption studies of water interactions with Apollo lunar samples 12001 and 72501. *Icarus* 255, 24–29.

Shimizu, K., A. E. Saal, C. E. Myers, A. N. Nagel, E. H. Hauri, D. W. Forsyth, V. S. Kamenetsky, and Y. Niu (2015), Two-component mantle melting-mixing model for the generation of mid-ocean ridge basalts: implications for the volatile content of the Pacific upper mantle, GCA.

Takir, D., Stockstill-Cahill, K. R., Hibbitts, C. A. & Nakauchi, Y., (2019), 3-μm reflectance spectroscopy of carbonaceous chondrites under asteroid-like conditions. *Icarus* 333, 243–251.

Watson, K., Murray, B.C., Brown, H., (1961), The behavior of volatiles on the lunar surface. *Journal of Geophysical Research*. Sep;66(9):3033-45.

Williams, J.P., Paige, D.A., Greenhagen, B.T., Sefton-Nash, E., (2017), The global surface temperatures of the Moon as measured by the Diviner Lunar Radiometer Experiment. *Icarus*. Feb 1;283:300-25.

Young, E.T., Becklin, E.E., Marcum, P.M., Roellig, T.L., De Buizer, J.M., Herter, T.L., Güsten, R., Dunham, E.W., Temi, P., Andersson, BG, Backman, D., (2012), Early science with SOFIA, the stratospheric observatory for infrared astronomy. *The Astrophysical Journal Letters.* Mar 29;749(2):L17.

Zeller, E. J., Ronca, L. B., & Levy, P. (1966). Proton-induced hydroxyl formation on the lunar surface. Journal of Geophysical Research, 71(20), 4855–4860. https://doi.org/10.1029/JZ071i020p04855

Zhu, C. et al. (2019), Untangling the formation and liberation of water in the lunar regolith. *Proc. Natl Acad. Sci.* USA 116, 11165–11170.

Geophysical Research Letters

Supporting Information for

Regional map of molecular water at high southern latitudes on the Moon using 6 µm data from the Stratospheric Observatory For Infrared Astronomy

C. I. Honniball[1], P. G. Lucey[2], A. Arrendando[3], W. T. Reach[3] and E. R. Malaret[4]

[1]NASA Goddard Space Flight Center, Greenbelt, MD, USA. [2]Hawai‘i Institute of Geophysics and Planetology, University of Hawai‘i at Mānoa, Honolulu, HI, USA. [3]NASA Ames Research Center, Moffett Field, CA, USA. [4]Applied Coherent Technology, Herndon, VA, USA.

Corresponding author: Casey Honniball (casey.i.honniball@nasa.gov)

Contents of this file

Figures S1 to S3
Tables S1

1. Extended methods

The wavelength is normally done by matching emission lines in spectra of supernovae to the target spectra. However, only a small number of lines are available for matching which causes a misalignment in the wavelength calibration of our Moon data. This in turn caused the atmospheric removal procedure to leave behind artifacts that may confuse the final spectrum or cause shifts in the 6 µm band center. We took advantage of the fact that the Moon is bright to create a new wavelength calibration by matching atmospheric absorption lines in each spectrum. The new wavelength calibration allows for more accurate atmospheric removal without residual artifacts and for accurate characterization of the 6 µm band center.

During the calibration process is the correction of crosstalk that results in a linear pattern of bars spaced by 16 pixels, known as “jailbars” (Clark et al., 2021). Normal pipeline procedures remove the jailbars so that they are no longer observed in the flux calibrated data. However, for lunar observations we must remove a continuum from the flux to characterize the 6 µm band and in doing so we reveal residual jailbar artifacts that cause spikes in the spectra that may interfere with the 6 µm band. To correct the jailbar residuals we mask the jailbars in the raw data before running the SOFIA pipeline. This greatly reduces the jailbar residuals observed in the final spectra.

The radiometric calibration of the data is completed using recent observation of a standard star with known flux. For these observations the standard star Alpha Bootes was used. Finally after atmospheric removal (Lord, 1992), correction of residual artifacts, and the radiometric calibration the data are in units of flux (Jy). We then follow the methods of Honniball et al. (2020) to remove a remaining multiplicative artifact using the reference data and remove a continuum to convert the data to apparent emissivity.

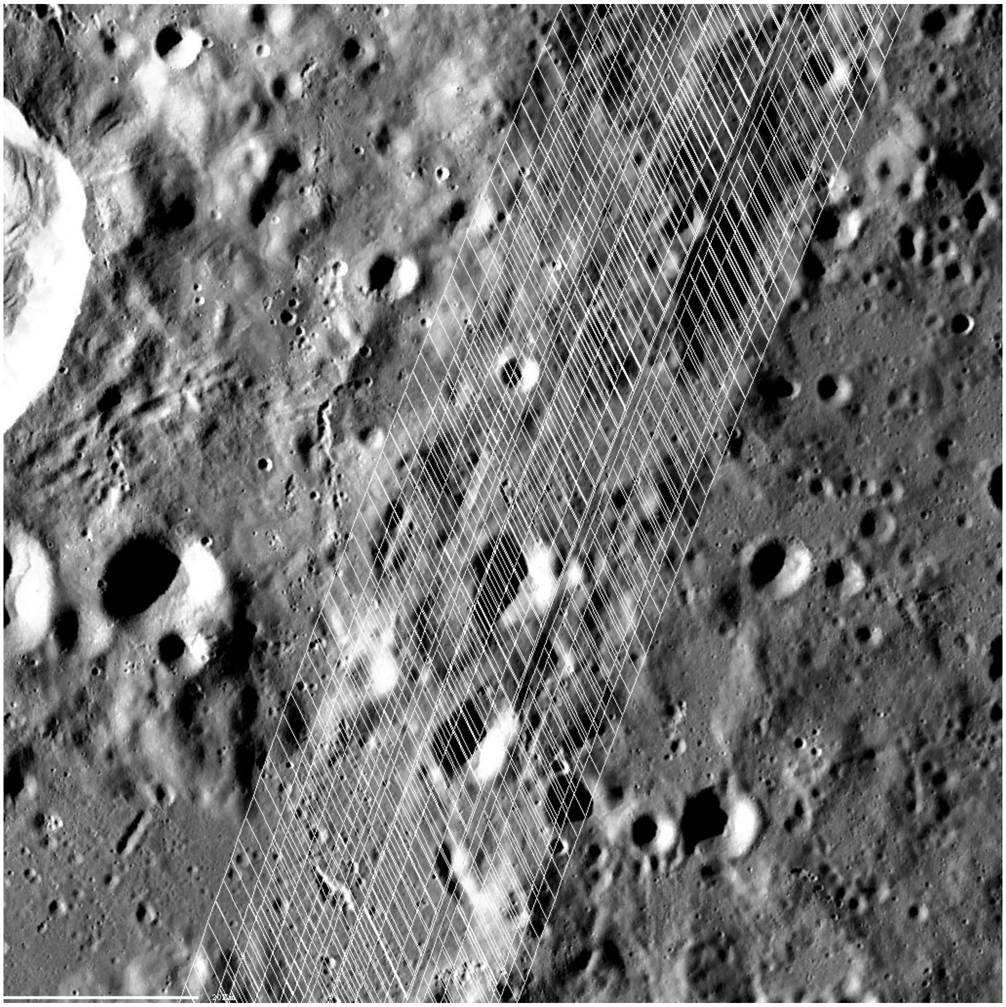

Figure S1: Closeup of mapped location of data pixels on the lunar surface.

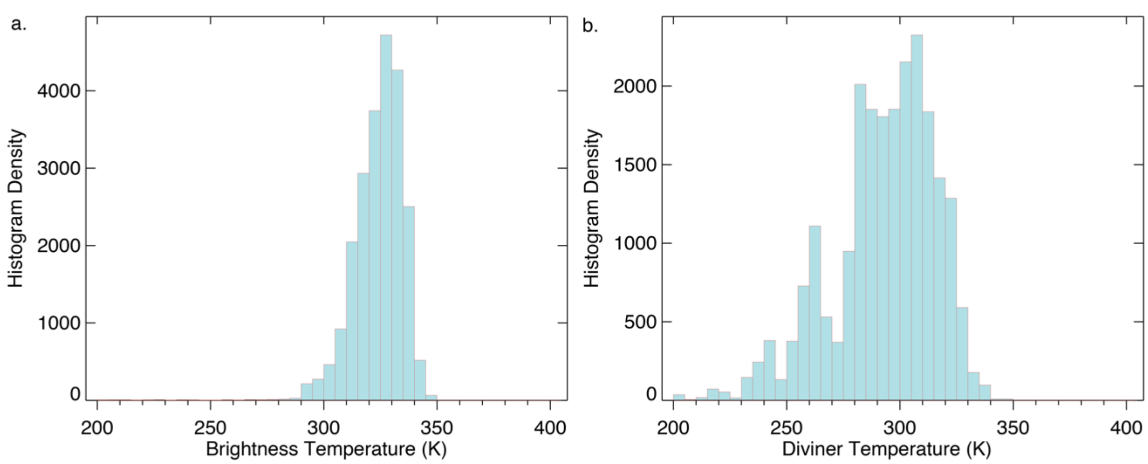

Figure S2: a.) Brightness temperature from the Moretus region. b.) Bolometric temperature from the LRO Diviner Lunar Radiometer for the same location and lunar time of day as the SOFIA Moretus data.

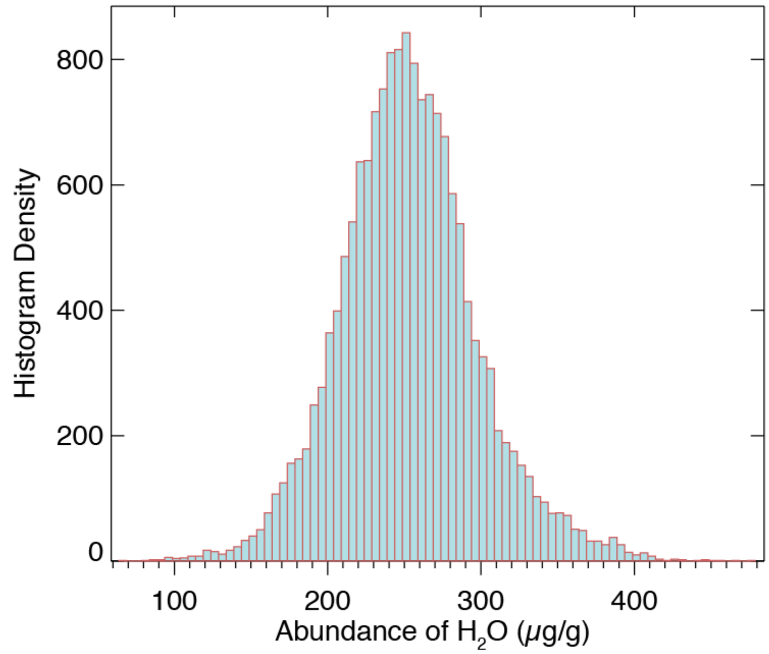

Figure S3: Distribution of water concentrations for the Moretus region.

Table S1: Flight conditions of each scan during the SOFIA flight FO751. Start values are taken from the beginning frame in the scan and the end values are from the ending frame in the scan. Values are quired from the file header information and the start value is used (example: for file 76 the start altitude is taken from the keyword 'ALTI_STA' in the header information).

Target		**Moretus Region**			
Scan		**1**	**2**	**3**	**4**
File Numbers		76-100	110-139	146-175	184-193
Integration time (s)		8.6			
UT 2021-06-23	Start	06:06:02.86	06:53:14.02	07:32:21.57	08:20:54.61
	End	06:19:44.79	07:17:20.35	07:56:36.27	08:25:45.16
Altitude (ft)	Start	40015	40009	41009	42022
	End	40015	40020	41020	42014
Aircraft Latitude	Start	37.5842	36.5515	35.9912	35.387
	End	37.2546	36.178	35.7605	35.2991
Aircraft Longitude	Start	-124.969	-132.825	-139.274	-147.601
	End	-127.266	-136.791	-143.339	-148.436
Zenith Angle	Start	61.7135	60.3351	59.6047	58.949
	End	61.2346	59.8277	59.3162	58.8755
Lunar Latitude	Start	-60.08	-61.17	-61.01	-55.11
	End	-58.12	-60.40	-57.49	-58.94

Lunar Longitude	Start	6.16	6.47	3.29	3.16
	End	62.72	18.99	14.81	-3.75

Target		**Mare Reference**			
Scan		**1**	**2**	**3**	**4**
File Numbers		101-108	140-145	176-183	194-203
Integration time (s)		8.6			
UT 2021-06-23	Start	06:29:14.88	07:22:12.76	07:26:33.22	08:27:37.35
	End	06:45:04.01	07:27:05.71	08:13:55.63	08:35:02.18
Altitude (ft)	Start	40014	40014	40014	42018
	End	40006	40015	41020	42026
Aircraft Latitude	Start	37.0349	36.1121	36.0571	35.2661
	End	36.7053	36.0571	35.5078	35.1343
Aircraft Longitude	Start	-128.837	-137.582	-138.307	-148.755
	End	-131.462	-138.395	-146.349	-150.007
Zenith Angle	Start	60.6286	59.408	59.3415	58.5233
	End	60.1868	59.3427	58.7471	58.4203
Lunar Latitude	Start	-1.58	-0.29	-0.07	-0.92
	End	-1.96	-1.57	-0.84	-1.28
Lunar Longitude	Start	59.11	58.97	57.83	55.73
	End	73.06	55.11	54.8	55.05